AGU PUBLICATIONS

Geophysical Research Letters

RESEARCH LETTER

10.1002/2017GL072726

Seismic tomography of the North Anatolian Fault: New insights into structural heterogeneity along a continental strike-slip fault

Elvira Papaleo[1], **David G. Cornwell**[1], **and Nicholas Rawlinson**[1]

[1] School of Geosciences, University of Aberdeen, King's College, Aberdeen, UK

Key Points:

- High-resolution (12 km) teleseismic tomography of the North Anatolian Fault
- Clear evidence for along-strike variation in the structure of the deep crust
- Simple model of narrow fault zone widening with depth applicable to the NAFZ

Supporting Information:

- Supporting Information S1
- Movie S1

Correspondence to:
E. Papaleo,
elvira.papaleo@abdn.ac.uk

Citation:
Papaleo, E., D. G. Cornwell, and N. Rawlinson (2017), Seismic tomography of the North Anatolian Fault: New insights into structural heterogeneity along a continental strike-slip fault, *Geophys. Res. Lett.*, *44*, 2186–2193, doi:10.1002/2017GL072726.

Received 19 JAN 2017
Accepted 21 FEB 2017
Accepted article online 24 FEB 2017
Published online 11 MAR 2017

Abstract Knowledge of the structure of continental strike-slip faults within the lithosphere is essential to understand where the deformation occurs and how strain localizes with depth. With the aim to improve the constraints on the lower crust and upper mantle structure of a major continental strike-slip fault, we present a high-resolution teleseismic tomography of the North Anatolian Fault Zone (NAFZ) in Turkey. Our results highlight the presence of a relatively high velocity body between the two branches of the fault and significant along-strike variations in the NAFZ velocity structure over distances of ~20 km. We interpret these findings as evidence of laterally variable strain focussing caused by preexisting heterogeneity. Low velocities observed in the crust and upper mantle beneath the NAFZ support the presence of a narrow shear zone widening in the upper mantle, where we constrain its width to be ~50 km.

1. Introduction

Continental strike-slip faults can extend for hundreds of kilometers and accommodate slip rates of up to 40 mm/yr [*Molnar and Dayem*, 2010]. However, despite their size and importance in global plate tectonics, their deep structure, key to understanding strain localization with depth and the characteristics of the seismic cycle, is poorly understood. Geological and geophysical evidence from major ancient and active fault zones [e.g., *Sibson*, 1977; *Vauchez et al.*, 1995; *Pili et al.*, 1997] indicates that they are not confined to the (brittle) seismogenic layer but extend deeper into the ductile crust and possibly the upper mantle. Studies of some present-day examples such as the San Andreas, Altyn Tagh, and Alpine Faults also provide evidence that they are rooted in the upper mantle [e.g., *Fuis et al.*, 2012; *Wittlinger et al.*, 1998; *Karalliyadda and Savage*, 2013].

A key debate concerns variations in fault zone width (defined here as the region of influence of the fault in the crust and upper mantle) as a function of depth in the continental lithosphere, with estimates at the near surface of <10 km to tens of kilometers in the lower crust and up to several hundreds of kilometers in the lithospheric mantle [e.g., *Platt and Behr*, 2011, and references therein]. Various models have been proposed to understand the structure of continental shear zones in the lower crust and upper mantle (e.g., *Sibson* [1983], *Molnar et al.* [1999], *Regenauer-Lieb et al.* [2006], or *Norris and Toy* [2014] for a review). These models span a wide range of possibilities and include (1) a narrow fault zone that crosscuts the entire lithosphere, possibly widening with depth, (2) narrow crustal fault zones underlain by broadly distributed shear that may extend into the upper mantle, and (3) fault zones that include a detachment at lower crust or deeper levels. No single model currently explains all observations at active continental strike-slip faults or geological evidence from ancient fault zones, and therefore, more detailed analyses of continental lithosphere bisected by such a fault zone are required. In this context, we constrain the deep structure of the North Anatolian Fault Zone (NAFZ) in northwestern Anatolia using teleseismic tomography and produce a detailed 3-D velocity model of the crust and upper mantle that highlights the complex structure of an active strike-slip plate boundary.

The NAFZ is a dextral strike-slip fault that has variously been estimated at between 1200 and 1500 km in length, nucleates at the Karliova triple junction, crosses the Anatolian Peninsula to the north, and reaches the Aegean Sea, where it splays into multiple strands [e.g., *Barka*, 1992; *Le Pichon et al.*, 2016]. Relative motion along the fault is driven by collision of the Arabian plate to the east and subduction along the Hellenic Arc to the west [*Reilinger et al.*, 1997], although more recent studies [e.g., *Flerit et al.*, 2004; *Bulut et al.*, 2012a] suggest that the present-day motion of the Anatolian Peninsula is predominantly driven by subduction along the Hellenic Arc. The NAFZ is thought to have formed by progressive strain localization in a westerly widening

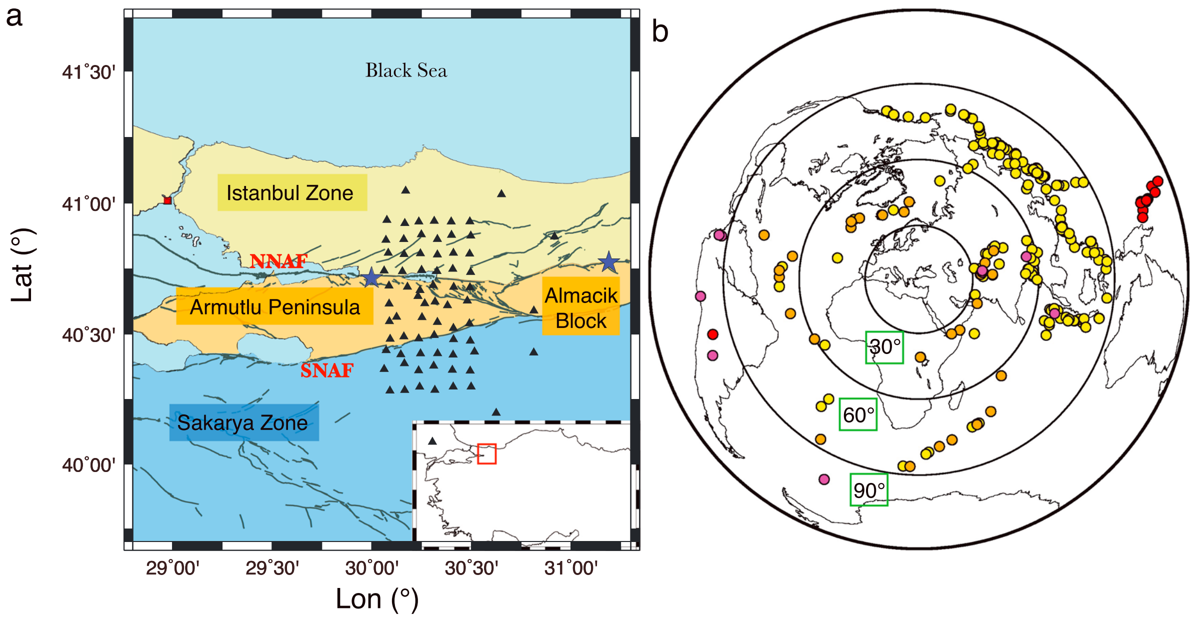

Figure 1. (a) Map of the study area with station locations and surface fault traces. The three main geological units in the area, the Istanbul Zone, the Armutlu Peninsula, and Almacık Block, and the Sakarya Zone are highlighted in yellow, orange, and blue, respectively. The red square marks the position of Istanbul, while the two blue stars indicate the epicenters of the 1999 Izmit and Düzce events. The inset on the bottom right shows the location of our study. (b) The locations of the events used for teleseismic tomography. Yellow dots represent earthquakes of $M_b \geq 5.5$ from which direct *P* arrivals are extracted; orange dots earthquakes of $4.5 \leq M_b < 5.5$ from which direct *P* arrivals are extracted; purple dots represent earthquakes from which *PP* or *PcP* arrivals are extracted, and red dots represent earthquakes from which *PKiKP* arrivals are extracted.

shear zone that bounds ancient continental basement to the north and subduction-accretion material of the Tethysides to the south [e.g., *Şengör et al.*, 2005]. It is seismically active with evidence for a recurrent series of migrating high-magnitude earthquakes that progressively activate adjacent NAFZ segments [*Stein et al.*, 1997], most recently at Izmit and Düzce in 1999 (see Figure 1 for the location of the latest 1999 events and *Bohnhoff et al.* [2016] for a more comprehensive review). The NAFZ splays into northern and southern strands (herein NNAF and SNAF, respectively) in our study region; the two strands separate different geological terranes, the Istanbul and Sakarya Zones, and bound a crustal block (Armutlu Block) of mixed provenance comprising Jurassic and pre-Jurassic units (similar to the Sakarya Zone) with metamorphic rocks of unknown age and provenance [*Okay and Tüysüz*, 1999](Figure 1).

Previous regional studies do not agree on the upper mantle seismic signature of the NAFZ in northwestern Anatolia. *Biryol et al.* [2011], using teleseismic tomography, constrained a ~4% faster *P* wave velocity upper mantle to the north (Istanbul Zone), compared with the south (Sakarya Zone), of the NAFZ. In contrast, *Fichtner et al.* [2013] and *Govers and Fichtner* [2016], using full waveform inversion, imaged a 50–100 km wide band of slow *S* wave velocities extending from 60 to 300 km depth to the east of 32°E longitude but no such signature beneath the NAFZ farther west. In order to image the NAFZ as it bisects the Anatolian lithosphere on a more local scale with improved horizontal resolution, a dense network of broadband seismic stations (DANA, Dense Array for Northern Anatolia, [*DANA*, 2012]) was deployed on the western segment of the fault where it splits in two major fault branches (NNAF and SNAF, Figure 1). We find supporting evidence for localized shear zones beneath the NAFZ that may penetrate the upper mantle with varying along-strike characteristics and discuss our findings in relation to applicable fault models, strain focussing, and the reactivation of inherited structures.

2. Data and Method

Teleseismic events used in the tomography study were recorded during the period of deployment of the DANA array (May 2012–October 2013), which comprised 73 broadband stations with a 7 km nominal spacing (Figure 1a). A total of 14,183 arrival time residuals from 263 events were used, most of which were direct *P* arrivals with $M_w \geq 5.5$, restricted to angular distances between 27° and 98° to avoid triplications caused by mantle discontinuities. We included 37 $4.5 \leq M_w < 5.5$ events and a total of 27 *PP*, *PcP*, and *PKiKP* identified phases to increase the azimuthal coverage of our data set to the south and west (Figure 1b).

Relative arrival time residuals were obtained using the adaptive stacking code of *Rawlinson and Kennett* [2004], which is particularly effective in this setting as it exploits the interstation coherence of teleseismic waveforms. Prior to stacking, waveforms were filtered between 0.4 and 5.0 Hz and approximately aligned using *ak*135 predicted arrival times [*Kennett et al.*, 1995]. The results of the stacking procedure were visually checked to eliminate noisy stations and ensure good quality picks. Relative arrival time residuals were inverted using the Fast Marching Teleseismic Tomography Package [*Rawlinson et al.*, 2006a], an iterative method combining the Fast Marching Method [*Sethian*, 1999] to track the evolving wavefront interface from the base of the model to the receivers and a subspace inversion method to solve the inverse problem [*Kennett et al.*, 1988]. The 3-D volume beneath the receiver array was parameterized using cubic *B* spline volume elements whose values are controlled by a mesh of velocity nodes in spherical coordinates [*Rawlinson et al.*, 2006b]. The initial velocity model was modified from *ak*135 by increasing Moho depth to 37 km and using a crustal velocity model more relevant to our study area [*Karahan et al.*, 2001; *Vanacore et al.*, 2013; *Kahraman et al.*, 2015] (supporting information Table S1 and Figure S1). Smoothing and damping parameters required by the inversion procedure were calibrated in order to obtain the optimum trade-off between data fit, model perturbation (relative to the starting model), and model roughness (see supporting information Figure S2 for trade-off curves).

To assess the resolution and quality of our inversion results, we performed synthetic checkerboard and spike tests. Checkerboard tests (supporting information Figures S3 and S4) show good recovery of the velocity anomalies in pattern and amplitude, especially beneath the area covered by the array, where the smallest checkerboard anomaly able to be recovered confidently is $12 \times 12 \times 12$ km. Spike tests (supporting information Figure S5) reveal good recovery of a single 12×12 km anomaly at 70 km depth with negligible horizontal smearing but a 70% loss in amplitudes. Vertical smearing is estimated at ± 3 to ± 5 km in areas with good data coverage and less than ± 10 km at the edges of our resolved area. We note that in our model the Moho is assumed to be flat and represented by a strong velocity gradient; this is most likely not the case as the Moho has been shown to have up to 8 km of topography by other studies [e.g., *Frederiksen et al.*, 2015; *Taylor et al.*, 2016]. Lateral variations in Moho depth will be mapped as relatively fast anomalies above the input Moho when the crustal thickness is reduced and as relatively slow anomalies below the input Moho when the crustal thickness is increased. To assess the effect of two such anomalies in our model, we performed an additional spike test to simulate the presence of a step in the Moho (supporting information Figure S6). This test shows that horizontal smearing is less than 2 km; however, vertical smearing at lower crust and upper mantle depths may be as much as ± 8 km. In summary, we are confident that our inversion results are robust and that primary velocity anomalies represent geological variations throughout the crust and upper mantle.

3. Tomographic Model

We show velocity anomalies relative to a background model (supporting information Table S1) for north-south profiles at longitudes of 30.5, 30.3, and 30.1°E (Figure 2). The profiles are within an area beneath recording stations where horizontal and vertical resolution is estimated to be ≤ 12 km. Common features can be identified between adjacent profiles, with the most evident being a ≥ 200 m/s fast velocity anomaly (labeled “A” in Figure 2) between the two NAFZ branches. This fast anomaly appears to be confined to the upper crust (<15 km depth) in the west of our model but extends into the upper mantle (and therefore increases in volume and significance) farther east. The surface expression of the NNAF (red triangle in Figure 2) occurs at the interface between the fast anomaly A and a slow velocity anomaly, “B”, to the north, while the surface trace of the southern NAFZ (blue triangle in Figure 2) is situated above the slowest velocity (-250 m/s) anomaly observed in our model. Slow velocity (-100 to -200 m/s) anomaly B extends in depth for ~ 80 km from the surface to the upper mantle below and immediately north of the NNAF, although it may be confined to the crust in the westernmost profile (Figure 2c). The extension of slow velocity anomaly B, where it can be identified below the Moho, typically has a NAFZ-perpendicular width of 30–50 km. The prominent slow velocity (-100 to -250 m/s) anomaly that lies below and immediately south of the SNAF (labeled “C” in Figure 2) is wider at >25 km throughout the crust than its counterpart beneath the NNAF and also extends in depth for ~ 80 km from the surface to the upper mantle in the westernmost profile, again with a NAFZ-perpendicular width of 30–50 km (Figure 2c). The relationship between slow velocity anomalies B and C is complex, but they may be connected at progressively deeper levels from west (Figure 2c) to east (Figure 2a).

We clearly observe a prominent change in the general pattern of velocity anomalies as we transition from upper crust to the upper mantle in our depth slices (Figure 3 and Movie S1 in supporting information).

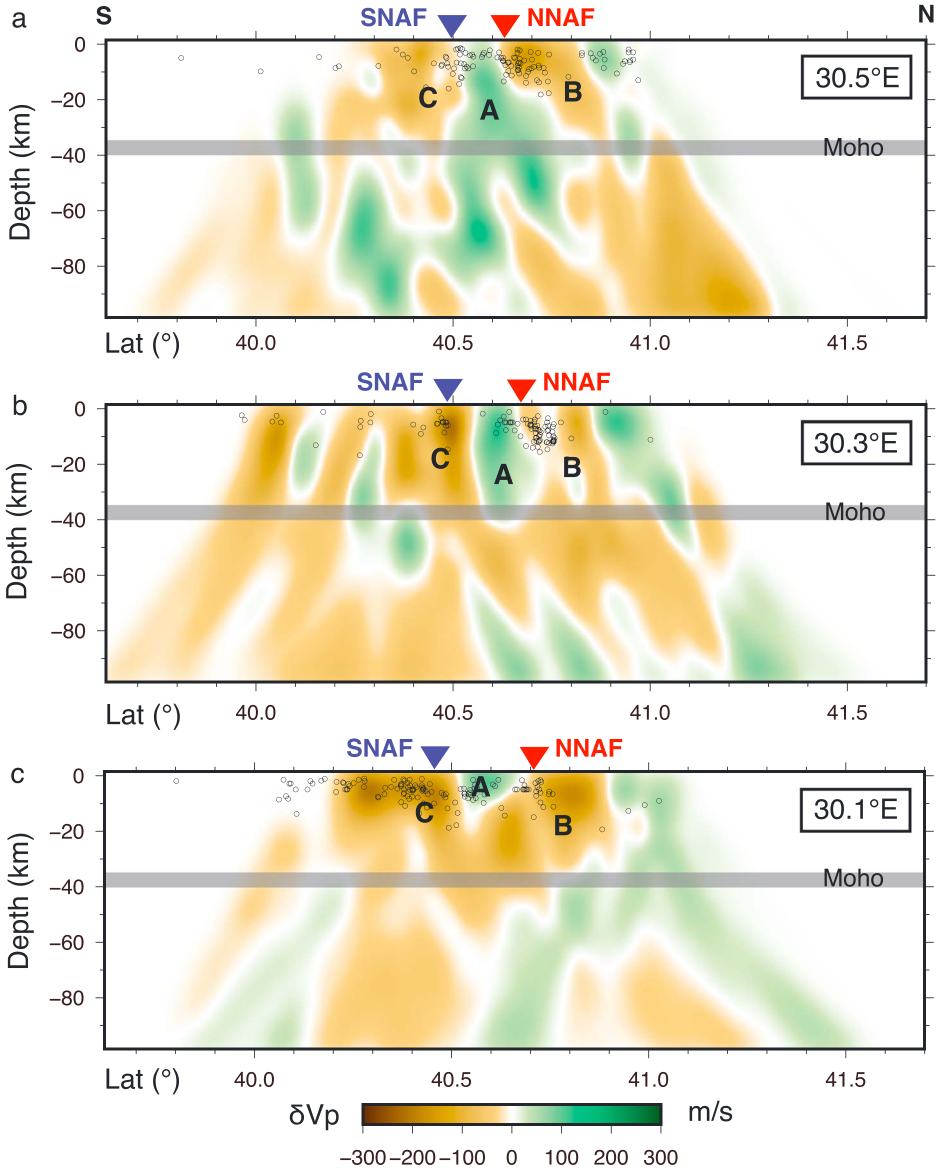

Figure 2. (a–c) Vertical profiles through the 3-D model with local seismicity recorded during the period of deployment of the DANA array [*Altuncu Poyraz et al.*, 2015] between ±0.05° from the profile plotted as circles. The gray line indicates the approximate depth of the Moho; red and blue triangles represent the surface locations of the northern and southern branches of the NAFZ, respectively. The letters A, B, C, denote anomalies discussed in the text.

Comparing depth slices at 15 and 60 km shows that the majority of velocity anomalies trend east-west and broadly NAFZ-parallel in the upper crust (Figure 3a) and north-south to northeast-southwest below the Moho (Figure 3c). The general pattern of velocity anomalies is less clear in the lower crust (Figure 3b).

4. Discussion

Slow upper crustal velocities have been attributed, depending on the geological context, to different causes, such as the presence of deep sedimentary basins, brittle deformation, grain size and/or lithological variations, positive temperature anomalies, and presence of fluids [e.g., *Bourjot and Romanowicz*, 1992; *Miller and Smith*, 1999; *Schurr et al.*, 2006]. In the studied area, these relatively low velocities are most likely to be the result of brittle deformation caused by the NAFZ, lithological variations [e.g., *Okay and Tüysüz*, 1999], and positive temperature anomalies [e.g., *Ilkışık*, 1995]. It is difficult to assess the relative contributions of these factors; however, we observe that the majority of local seismicity recorded during the 18 month DANA deployment

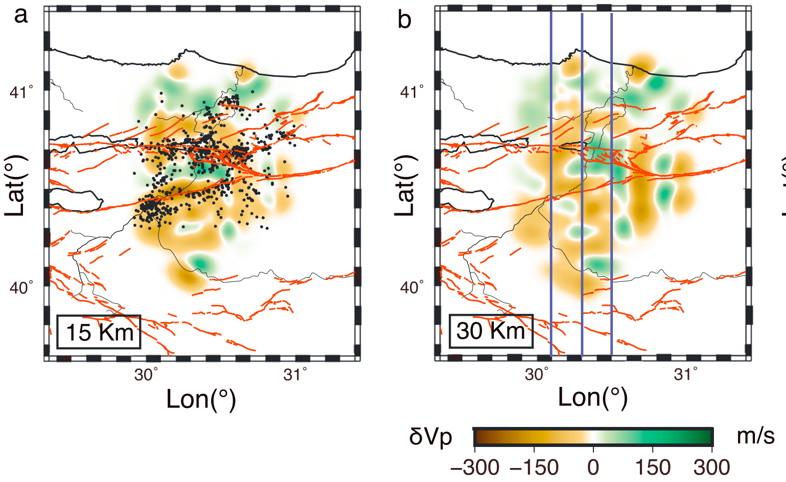

Figure 3. Horizontal slices through the 3-D model. (a) Depth slice at 15 km; black dots are local seismicity [*Altuncu Poyraz et al.*, 2015]. (b) Depth slice at 30 km; blue lines indicate the position of the profiles in Figure 2. (c) Depth slice at 60 km; black triangles are the station locations of the DANA array.

[*Altuncu Poyraz et al.*, 2015] occurred within relatively slow upper crust and, in particular, is concentrated where we observe the strongest lateral velocity contrasts beneath the NNAF where it ruptured during the 1999 Izmit earthquake (Figures 3a and 4). Similarly, the presence of velocity contrasts across segments of the NAFZ in close proximity to our study area has also been documented by *Bulut et al.* [2012b] and *Najdahmadi et al.* [2016] who looked at fault head waves generated by the presence of a bimaterial interface.

Furthermore, our results agree with a ∼7% reduction in *P* wave velocity and increase in attenuation beneath the NNAF constrained by local earthquake tomography [*Koulakov et al.*, 2010], and therefore, we infer that the relatively low velocity region in the crust beneath the NNAF and the minor faults in its close proximity most likely represents a narrow (∼25 km) corridor of brittle deformation associated with ongoing NAFZ shearing. The relatively low velocities observed throughout the Sakarya terrane in our model make it difficult to constrain an area of brittle deformation caused by the SNAF, and, despite not excluding its existence, it is possible that low velocities with respect to the background model are a characteristic of the upper crust in the Sakarya tarrane.

The relatively high velocity body bounded by the NNAF and SNAF coincides with surface outcrops of Neo-Proterozoic basement, a Lower Cretaceous accretionary complex and an Upper Cretaceous tectonic melange. This heterogeneous crustal block, originally part of the Almacik Block in the east [*Akbayram et al.*, 2016], most likely represents a locally resistant/strong block that localizes strain at its margins and in adjacent rheologically weaker domains [e.g., *Tommasi et al.*, 1995; *Dayem et al.*, 2009]. Such relatively weak regions could correspond to a midcrustal low-viscosity zone required to model deformation before and after the 1999 Izmit earthquake [*Yamasaki et al.*, 2014]. Magnetotelluric studies in the region [*Tank et al.*, 2005; *Kaya*, 2010]

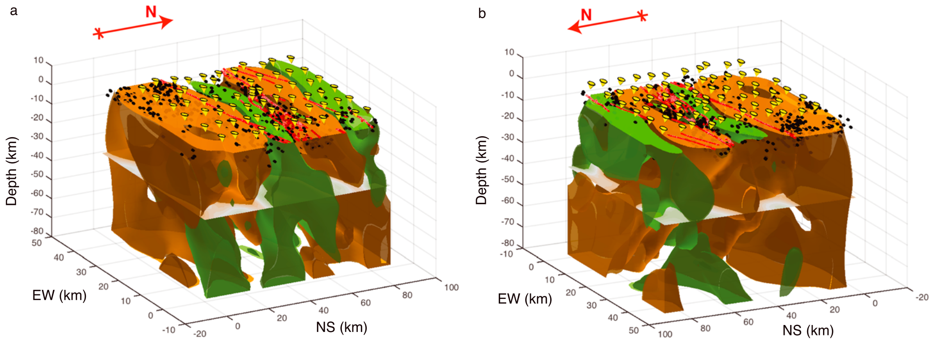

Figure 4. Three-dimensional data volume seen from the (a) southeast and (b) northwest. Surface traces of the faults are drawn in red, the yellow cones indicate station locations, and the black spheres show the local seismicity within the volume [*Altuncu Poyraz et al.*, 2015]. The horizontal slice at 37 km depth in the data volume shows the approximate location of the Moho.

point to the presence of mildly conductive to conductive zones at middle and lower crustal level in close proximity to the NAFZ. In particular, *Tank et al.* [2005] image a conductive body between the NNAF and SNAF extending from 30 to 50 km depth and interpret it as indicative of partial melting causing pore pressure buildup during the interseismic period. We also note that in this study, *Tank et al.* observe a clear resistivity contrast across the NNAF that coincides with the contrast in velocity anomalies that we image with teleseismic tomography.

Our velocity images allow the structural elements that comprise the NAFZ to be traced from the brittle upper crust to the ductile regimes of the lower crust and upper mantle. We find that the NNAF represents a narrow but more diffuse (30–50 km) shear zone in the upper mantle than in the upper crust (∼25 km). Such a narrow shear zone is consistent with the observations from colocated receiver function and autocorrelation studies that mapped abruptly terminating crust and Moho discontinuities in the proximity of the NNAF [*Kahraman et al.*, 2015; *Taylor et al.*, 2016]. It is less clear, but the shear zone may be narrowest in the lower crust. A localized shear zone in a similar setting beneath the active Altyn Tagh strike-slip fault was also interpreted from slow velocity anomalies [*Wittlinger et al.*, 1998]. Relatively low velocities beneath the SNAF are less focussed and mostly confined to the crust except in the westernmost part of our model, where we find evidence of a low velocity region in the upper mantle. This, coupled with the lack of a clear termination of the Moho signal in proximity of the SNAF [*Kahraman et al.*, 2015; *Taylor et al.*, 2016] suggests that the presence of a shear zone beneath this branch of the fault is less likely. Taking into account the lower slip rate on the SNAF (∼5–10 mm/yr as opposed to the ∼25 mm/yr of the NNAF [*Meade et al.*, 2002]) and the fact that the NNAF is also exploiting the presence of the old Intrapontide Suture Zone [*Şengör and Yilmaz*, 1981], we conclude that the SNAF localizes shear less effectively than the NAFZ.

The markedly different patterns of velocity anomalies observed outside the NNAF and SNAF relatively low velocities (Figure 2) may indicate that the Moho represents both a significant compositional and seismological discontinuity in the study region. The observation of northeast-southwest aligned upper mantle compared to east-west aligned upper crustal velocity anomalies may hint at a possible decoupling between shallow and deep parts of the lithosphere. However, an apparent ∼20 km offset or curvature in the prominent fast region that dominates the upper mantle in the east of Figure 3c may be interpreted as ductile deformation of a preexisting mantle structure by ongoing NAFZ shear. Further investigations are needed to confirm this hypothesis, which, if verified, would predict that a quarter to a third of the observed NNAF surface displacement exists in the upper mantle and that the brittle and ductile parts of the deforming lithosphere are only partially coupled.

Our velocity data suggests that the most plausible tectonic model for the NNAF is that of a narrow shear zone that crosscuts the entire crust and widens slightly in the upper mantle, while the SNAF may have a more complex structure, also influenced by the extensional tectonic of the region. Moreover, we reveal that both NAFZ strands are characterized by along-strike variations over short length scales (<20 km), and our interpretation is that these variations point to preexisting heterogeneity playing a major role in strain localization on a local scale. The best example of this in our study region is the relatively high velocity block offset by the NNAF and acting as a wedge of locally strong lithosphere around which the two branches of the NAFZ propagate.

5. Conclusions

We have applied teleseismic tomography to data recorded by a dense seismological array of 73 stations and show that we can image both crust and upper mantle (to ∼80 km depth) of a complex shear zone with a horizontal and vertical resolution of ∼12 km.

Our 3-D velocity model of the area shows a heterogeneous lithosphere beneath the NAFZ, consistently with the complex tectonic history of the region. The low-velocity anomalies in the crust and upper mantle observed beneath the NNAF support the idea that the fault zone can be compared to the simple model of a narrow shear zone that widens in the upper mantle, where we constrain its north-south dimension to be 30–50 km; it is less clear whether a similar model can be applied to the SNAF as well. We demonstrate that both NNAF and SNAF are characterized by significant along-strike variations in their velocity structure, which we interpret as local differences in strain localization influenced by preexisting heterogeneity. In particular, the high velocity body situated between the two strands of the fault (and originally part of the Almacik Block to the west) is likely to be a crustal block more resistive to strain around which the NAFZ branches propagate. Clear variations in the pattern of velocity anomalies above and below Moho depth suggest that there is a decoupling between these layers, although the curvature we observe in the fast region of the upper mantle beneath the NNAF, if verified through other studies, would indicate that some degree of displacement caused by the fault also exists in the upper mantle.

Acknowledgments
DANA (Dense Array for Northern Anatolia) is part of the Faultlab project, a collaborative effort by the University of Leeds, Boğaziçi University Kandilli Observatory and Earthquake Research Institute (BU-KOERI), and Sakarya University. Major funding was provided by the UK Natural Environment Research Council (NERC) under grant NE/I028017/1. Equipment was provided and supported by the NERC Geophysical Equipment Facility (SEIS-UK). This project is also supported by Boğaziçi University Scientific Research Projects (BAP) under grant 6922 and Turkish State Planning Organization (DPT) under the TAM project, number 2007K120610. We are indebted to the Faultlab seismological fieldwork team members Sebastian Rost, Greg Houseman, David Thompson, Sandra Karl, Luke Jackson, Hannah Bentham, Ekbal Hussain, Selda Altuncu Poyraz, Uğur Teoman, Niyazi Türkelli, Metin Kahraman, Murat Utkucu, and Levent Gülen. Victoria Lane (SEIS-UK) provided invaluable technical and practical seismological assistance. The seismic data set can be found in the references.

References

Akbayram, K., C. Sorlien, and A. I. Okay (2016), Evidence of a minimum 52 ± 1 km of total offset along the northern branch of the North Anatolian Fault in northwest Turkey, *Tectonophysics*, *668–669*, 35–41.

Altuncu Poyraz, S., et al. (2015), New constraints on micro-seismicity and stress state in the western part of the North Anatolian Fault Zone: Observations from a dense seismic array, *Tectonophysics*, *656*, 190–201.

Barka, A. A. (1992), The North Anatolian Fault Zone, *Ann. Tectonicae*, *6*, 164–195.

Biryol, C. B., S. L. Beck, G. Zandt, and A. A. Özacar (2011), Segmented African lithosphere beneath the Anatolian region inferred from teleseismic P-wave tomography, *Geophys. J. Int.*, *184*, 1037–1057.

Bohnhoff, M., P. Martínez-Garzón, F. Bulut, E. Stierle, and Y. Ben-Zion (2016), Maximum earthquake magnitudes along different sections of the North Anatolian Fault Zone, *Tectonophysics*, *674*, 147–165.

Bourjot, L., and B. Romanowicz (1992), Crust and upper mantle tomography in Tibet using surface waves, *Geophys. Res. Lett.*, *19*, 881–884.

Bulut, F., M. Bohnhoff, T. Eken, C. Janssen, T. Kılıç, and G. Dresen (2012a), The East Anatolian Fault Zone: Seismotectonic setting and spatiotemporal characteristics of seismicity based on precise earthquake locations, *J. Geophys. Res.*, *117*, B07304, doi:10.1029/2011JB008966.

Bulut, F., Y. Ben-Zion, and M. Bonhoff (2012b), Evidence for a bimaterial interface along the Mudurnu segment of the North Anatolian Fault Zone from polarization analysis of P waves, *Earth Planet. Sci. Lett.*, *327–328*, 17–22.

DANA (2012), *Dense array for Northern Anatolia*, doi:10.7914/SN/YH_2012. Other/Seismic Network.

Dayem, K. E., G. A. Houseman, and P. Molnar (2009), Localization of shear along a lithospheric strength discontinuity: Application of a continuous deformation model to the boundary between Tibet and the Tarim Basin, *Tectonics*, *28*, TC3002, doi:10.1029/2008TC002264.

Fichtner, A., E. Saygin, T. Taymaz, P. Cupillard, and Y. Capdeville (2013), The deep structure of the North Anatolian Fault Zone, *Earth Planet. Sci. Lett.*, *373*, 109–117.

Flerit, F., R. Armijo, G. King, and B. Meyer (2004), The mechanical interaction between the propagating North Anatolian Fault and the back-arc extension in the Aegean, *Earth Planet. Sci. Lett.*, *224*, 347–362.

Frederiksen, A. W., et al. (2015), Crustal thickness variations and isostatic disequilibrium across the North Anatolian Fault, western Turkey, *Geophys. Res. Lett.*, *42*, 751–757, doi:10.1002/2014GL062401.

Fuis, G. S., D. S. Scheirer, V. E. Langenheim, and M. D. Kohler (2012), A new perspective on the geometry of the San Andreas Fault in Southern California and its relationship with lithospheric structure, *Bull. Seismol. Soc. Am.*, *102*, 236–251.

Govers, R., and A. Fichtner (2016), Signature of slab fragmentation beneath Anatolia from full-waveform tomography, *Earth Planet. Sci. Lett.*, *450*, 10–19.

Ilkışık, O. M. (1995), Regional heat flow in western Anatolia using silica temperature estimates from thermal springs, *Tectonophysics*, *244*, 175–184.

Kahraman, M., D. G. Cornwell, D. A. Thompson, S. Rost, G. A. Houseman, N. Türkelli, U. Teoman, S. Altuncu Poyraz, M. Utkucu, and L. Gülen (2015), Crustal-scale shear zones and heterogeneous structure beneath the North Anatolian Fault Zone, Turkey, revealed by a high-density seismometer array, *Earth Planet. Sci. Lett.*, *430*, 129–139.

Karahan, A., H. Berckhemer, and B. Baier (2001), Crustal structure at the western end of the North Anatolian Fault Zone from deep seismic sounding, *Ann. Geophys.*, *44*, 49–68.

Karalliyadda, S. C., and M. K. Savage (2013), Seismic anisotropy and lithospheric deformation of the plate boundary zone in South Island, New Zealand: Inferences from local S-wave splitting, *Geophys. J. Int.*, *193*, 507–530.

Kaya, C. (2010), Deep crustal structure of northwestern part of Turkey, *Tectonophysics*, *489*, 227–239.

Kennett, B. N. L., M. Sambridge, and P. R. Williamson (1988), Subspace methods for large scale inverse problems involving multiple parameter classes, *Geophys. J. Int.*, *94*, 237–247.

Kennett, B. N. L., E. R. Engdahl, and R. Buland (1995), Constraints on seismic velocities in the Earth from traveltimes, *Geophys. J. Int.*, *122*, 108–124.

Koulakov, I., D. Bindi, S. Parolai, H. Grosser, and C. Milkereit (2010), Distribution of seismic velocities and attenuation in the crust beneath the North Anatolian Fault (Turkey) from local earthquake tomography, *Bull. Seismol. Soc. Am.*, *100*, 207–224.

Le Pichon, X., A. M. C. Şengör, J. Kende, C. İmren, P. Henry, C. Grall, and H. Karabulut (2016), Propagation of a strike-slip plate boundary within an extensional environment: The westward propagation of the North Anatolian Fault, *Can. J. Earth Sci.*, *53*, 1416–1439.

Meade, B. J., B. H. Hager, S. C. McClusky, R. E. Reilinger, S. Ergintav, O. Lenk, A. Barka, and H. Ozener (2002), Estimates of seismic potential in the Marmara Sea region from block models of secular deformation constrained by Global Positioning System measurements, *Bull. Seismol. Soc. Am.*, *92*, 208–215.

Miller, D. S., and R. B. Smith (1999), P and S velocity structure of the Yellowstone volcanic field from local earthquake and controlled-source tomography, *J. Geophys. Res.*, *104*, 15,105–15,121.

Molnar, P., et al. (1999), Continuous deformation versus faulting through the continental lithosphere: Tests using New Zealand as a laboratory for the study of continental dynamics, *Science*, *286*, 516–519.

Molnar, P., and K. Dayem (2010), Major intracontinental strike-slip faults and contrasts in lithospheric strength, *Geosphere*, *6*, 444–467.

Najdahmadi, B., M. Bonhoff, and Y. Ben-Zion (2016), Bimaterial interfaces at the Karadere segment of the North Anatolian Fault, northwestern Turkey, *J. Geophys. Res. Solid Earth*, *121*, 931–950, doi:10.1002/2015JB012601.

Norris, R. J., and V. G. Toy (2014), Continental transforms: A view from the Alpine Fault, *J. Struct. Geol.*, *64*, 3–31.

Okay, A. I., and O. Tüysüz (1999), Tethyan suture of northern Turkey, *Geol. Soc. London Spec. Publ.*, *156*, 475–515.

Pili, E., Y. Ricard, J.-M. Lardeaux, and S. M. F. Sheppard (1997), Lithospheric shear zones and mantle-crust connections, *Tectonophysics*, *280*, 15–29.

Platt, J. P., and W. M. Behr (2011), Deep structure of lithospheric fault zones, *Geophys. Res. Lett.*, *38*, L24308, doi:10.1029/2011GL049719.

Rawlinson, N., and B. L. N. Kennett (2004), Rapid estimation of relative and absolute delay times across a network by adaptive stacking, *Geophys. J. Int*, *157*, 332–340.

Rawlinson, N., A. M. Reading, and B. L. N. Kennett (2006a), Lithospheric structure of Tasmania from a novel form of teleseismic tomography, *J. Geophys. Res.*, *111*, B02301, doi:10.1029/2005JB003803.

Rawlinson, N., B. L. N. Kennett, and M. Heintz (2006b), Insights into the structure of the upper mantle beneath the Murray Basin from 3D teleseismic tomography, *Aust. J. Earth Sci.*, *53*, 595–604.

Regenauer-Lieb, K., R. F. Weinberg, and G. Rosenbaum (2006), The effect of energy feedbacks on continental strength, *Nature*, *442*, 67–70.

Reilinger, R. E., S. C. McClusky, M. B. Oral, R. W. King, M. N. Toksoz, A. A. Barka, I. Kinik, O. Lenk, and I. Sanli (1997), Global position system measurements of present-day crustal movements in the Arabia-Africa-Eurasia plate collision zone, *J. Geophys. Res.*, *102*, 9983–9999.

Schurr, B., A. Rietbrock, G. Asch, R. Kind, and O. Oncken (2006), Evidence for lithospheric detachment in the central Andes from local earthquake tomography, *Tectonophysics*, *415*, 203–223.

Şengör, A. M. C., and Y. Yilmaz (1981), Tethyan evolution of Turkey: A plate tectonic approach, *Tectonophysics*, *75*, 181–141.

Şengör, A. M. C., O. Tüysüz, C. İmren, M. Sakınç, H. Eyidoğan, N. Görür, X. Le Pichon, and C. Rangin (2005), The North Anatolian Fault: A new look, *Annu. Rev. Earth. Planet. Sci.*, *33*, 37–112.

Sethian, J. A. (1999), Fast marching methods, *SIAM Rev.*, *41*, 199–235.

Sibson, R. H. (1977), Fault rocks and fault mechanisms, *J. Geol. Soc. London*, *133*, 191–213.

Sibson, R. H. (1983), Continental fault structure and the shallow earthquake source, *J. Geol. Soc. London*, *140*, 741–767.

Stein, R. S., A. A. Barka, and J. H. Dieterich (1997), Progressive failure on the North Anatolian Fault since 1939 by earthquake stress triggering, *Geophys. J. Int.*, *128*, 594–604.

Tank, S. B., Y. Honkura, Y. Ogawa, M. Matsushima, N. Oshiman, M. K. Tunçer, C. Çelik, E. Tolak, and M. Işikara (2005), Magnetotelluric imaging of the fault rupture area of the 1999 İzmit (Turkey) earthquake, *Phys. Earth Planet. Inter.*, *150*, 213–225.

Taylor, G., S. Rost, and G. A. Houseman (2016), Crustal imaging across the North Anatolian Fault Zone from the autocorrelation of ambient seismic noise, *Geophys. Res. Lett.*, *43*, 2502–2507, doi:10.1002/2016GL067715.

Tommasi, A., A. Vauchez, and B. Daudré (1995), Initiation and propagation of shear zones in a heterogeneous continental lithosphere, *J. Geophys. Res.*, *100*, 22,083–22,101.

Vanacore, E. A., T. Taymaz, and E. Saygin (2013), Moho structure of the Anatolian Plate from receiver function analysis, *Geophys. J. Int.*, *193*, 329–337.

Vauchez, A., A. Neves, R. Caby, M. Corsini, M. Egydio-Silva, M. Arthaud, and V. Amaro (1995), The Borborema shear zone system, NE Brazil, *J. South Am. Earth Sci.*, *8*, 247–266.

Wittlinger, G., P. Tapponnier, G. Poupinet, J. Mei, S. Danian, G. Herquel, and F. Masson (1998), Tomographic evidence for localized lithospheric shear along the Altyn Tagh fault, *Science*, *282*, 74–76.

Yamasaki, T., T. J. Wright, and G. A. Houseman (2014), Weak ductile shear zone beneath a major strike-slip fault: Inferences from earthquake cycle model constrained by geodetic observations of the western North Anatolian Fault Zone, *J. Geophys. Res. Solid Earth*, *119*, 3678–3699, doi:10.1002/2013JB010347.